Energy & Environmental Science

Accepted Manuscript

This article can be cited before page numbers have been issued, to do this please use: F. Urbain, P. Tang, N. M. Carretero, T. Andreu, L. G. Gerling, C. Voz, J. Arbiol and J. R. Morante, *Energy Environ. Sci.*, 2017, DOI: 10.1039/C7EE01747B.

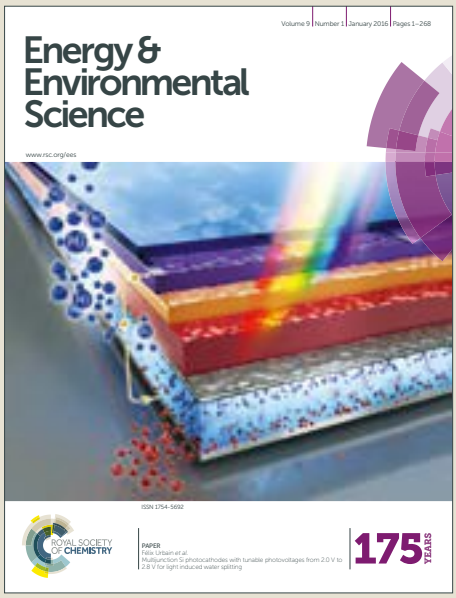

ROYAL SOCIETY OF CHEMISTRY

rsc.li/ees

View Article Online
DOI: 10.1039/C7EE01747B

Prototype reactor for highly selective solar-driven CO_2 reduction to synthesis gas using nanosized earth-abundant catalysts and silicon photovoltaics

Félix Urbain[1], Pengyi Tang[1,2], Nina M. Carretero[1], Teresa Andreu[1,5], Luis G. Gerling[3], Cristobal Voz[3], Jordi Arbiol[2,4], and Joan Ramon Morante[1,5]*

[1] IREC, Catalonia Institute for Energy Research, Jardins de les Dones de Negre 1, 08930 Sant Adrià de Besòs, Barcelona, Catalonia, Spain

[2] Catalan Institute of Nanoscience and Nanotechnology (ICN2), CSIC and The Barcelona Institute of Science and Technology (BIST), Campus UAB, Bellaterra, 08193 Barcelona, Catalonia, Spain

[3] Electronic Engineering Department, Universitat Politècnica de Catalunya, Jordi Girona 1–3, 08034 Barcelona, Catalonia, Spain

[4] ICREA, Pg. Lluís Companys 23, 08010 Barcelona, Catalonia, Spain

[5] Universitat de Barcelona, Martí i Franquès, 1, 08028 Barcelona, Catalonia, Spain

[*]**Corresponding author**: E-Mail: furbain@irec.cat

Abstract

The conversion of carbon dioxide (CO_2) into value-added chemicals and fuels, preferably using renewable energy and earth-abundant materials, is considered a key priority for future energy research. In this work, a bias-free reactor device for the solar-driven conversion of CO_2 to synthesis gas (syngas) has been developed. The integrated fluidic device consists of a cathode made of copper foam coated with low-cost nanosized zinc flakes as catalyst to perform the CO_2 reduction reaction (CO_2RR) to syngas, an adapted silicon heterojunction solar cell structure as photoanode with nickel foam as catalyst to facilitate the oxygen evolution reaction (OER), and a bipolar membrane separating the respective catholyte and anolyte compartments. The membrane allows for the operation of the catholyte and anolyte at different pH values. Stable and tunable hydrogen-to-carbon monoxide (H_2:CO) ratios between 5 and 0.5 along with high CO faradaic efficiencies of up to 85 % and CO current densities of 39.4 mA/cm^2 have been demonstrated. Under photoelectrolysis conditions, the photovoltage of the photoanode was varied between 0.6 V and 2.4 V by connecting up to four heterojunction solar cells in series and thus, reducing the overall cell voltage solely by solar energy utilization. Bias-free operation of the integrated device has been achieved at ambient conditions with active areas for CO_2RR and OER, respectively, of 10 cm^2. An operation current density of 5.0 mA/cm^2 was measured under 100 mW/cm^2 illumination of the complete device, which corresponds to a solar-to-syngas conversion efficiency of 4.3 %.

View Article Online
DOI: 10.1039/C7EE01747B

I. Introduction

Today's society is committed to reducing its greenhouse gas emissions substantially while encouraging others to do likewise. In the war against climate change, the consensus is that carbon dioxide (CO_2) capture and storage alone cannot solve this problem.[1,2] To have a meaningful effect, it is crucial to materialize chemical and catalytic processes that enable reusing CO_2 to convert it into value-added chemicals and fuels, preferably by using renewable and sustainable energy sources, such as solar energy. In spite of encouraging accomplishments in this field, yet substantial advances in the selection of cost-effective and earth-abundant materials enabling efficient photoabsorption and catalysis are needed to contribute to the climate change objectives.[3]

The main identified scientific challenges related to CO_2RR to form chemical fuels are the high overpotentials needed to perform the multi-electron transfers and the poor faradaic efficiency and product selectivity.[4] Among the various CO_2 reduction products, carbon monoxide (CO)[5], however, is a gaseous product, which requires only two electrons to be produced and thus, is accompanied by lower overpotentials, compared to methanol[6] or methane[7], for instance, which require the transfer of six and eight electrons to one molecule, respectively. Additionally, the concomitant hydrogen (H_2) production can be valorized to produce synthesis gas (syngas) which can be further processed and offers high optionality.[8] Providing tunable H_2:CO ratios is therefore highly desirable, as it makes syngas a versatile fuel precursor able to create the majority of the products and chemicals currently generated in the petrochemical industry, e.g. the synthesis of methanol via Fischer-Tropsch.[9,10] This two-step synthetic route using existing industrial processes is being perceived as more economically viable than the direct conversion of CO_2 into multi-electron products, such as methanol or ethylene, where also the subsequent product separation is highly energy-demanding.[11, 12]
Among the bulk metallic catalysts for CO production, silver (Ag)[13], gold (Au)[14], and zinc (Zn)[15-19], are identified as adequate candidates for selective CO_2-to-CO conversion. However, expensive elements, such as Ag or Au are not ideal for commercial applications at large scale (terawatt). In this regard, Zn represents a more satisfactory catalyst, as it is earth-abundant and significantly cheaper than other noble metal catalysts.
Besides the early work by Hori and Ikeda on bulk metallic Zn catalysts, recently also nanostructured Zn catalysts for CO_2 to CO conversion came to the fore among research groups. Dark electrochemical faradaic efficiencies up to 79 % and 93 % for cathodes based on nanosized dendrite[17] and flake Zn[18] catalyst structures, respectively, have been demonstrated.

However, so far, neither the viability of Zn as catalyst materials for selective syngas production, nor the applicability of a Zn-based cathode on a system-level, i.e. in a stand-alone device for solar-driven CO_2-to-fuel conversion combining electrochemical and photovoltaic structures has been hitherto demonstrated. Within this work we aimed to bridge that gap by addressing mainly three aspects:
We initiated our study with the Zn cathode material development. In particular we investigated the deposition of nanostructured Zn catalysts on highly conductive copper (Cu) foam using electrodeposition and evaluated its performance towards CO_2-to-syngas conversion along with the possibility to tune the H_2:CO ratios.
We subsequently focused on the adaption and integration of silicon (Si) heterojunction solar cells as photoanode to perform the oxygen evolution reaction (OER). The silicon heterojunction technology (HIT) was chosen herein as it stands out because it is non-

View Article Online
DOI: 10.1039/C7EE01747B

toxic, cheap, abundant, well understood, and has recently acquired an industry leading level.[20,21] Yet, the application of HIT cells as photoanodes for CO_2 conversion has not been reported previously and required meeting challenges, such as increasing the photovoltage without impairing the photovoltaic efficiency; protection of the solar cell to increase the stability in aqueous electrolytes; and the decoration with catalysts ensuring an efficient OER.[22-26] The latter was ensured by applying a nickel (Ni) foam on the rear side of the HIT cell as a three-dimensional catalyst.

Finally, we combined the optimized cathode and photoanode components in a single reactor assembly (large scale filter-press type electrochemical cell with 10 cm^2 active CO_2RR and OER areas, respectively) to perform the CO_2-to-syngas conversion using the sun as the only energy input, i.e. under bias-free working conditions. This reactor concept gives a push from the engineering side and thus, stands in contrast to the vast majority of laboratory approaches on solar-assisted CO_2 conversion, where only a few examples on prototyping devices exist.[27-30]

II. Experimental Section

A. Cathode preparation and structural characterization

Zinc catalysts were obtained by electrodeposition on copper foam using a two electrode cell configuration. A sheet of copper foam (cleaned in acetone and 2 M HCl) with a size of 40*40 mm^2 (geometrical area) was used as catalyst support and the counter electrode was a platinum mesh. The electrodeposition was conducted in a 1 M zinc sulfate ($ZnSO_4$) solution applying a constant current of -0.4 A for up to one hour at room temperature.[31] After electrodeposition, each electrode was thoroughly rinsed with deionized water and dried at room temperature. For comparison, a zinc foil (Alfa Aesar, 99.98%, 0.25 mm thick) cathode was also employed.

Structural characterization was carried out by X-ray diffraction (XRD). The samples were scanned from $2\theta = 20°$ to 80° at a rate of 0.02 s^{-1} in Bragg–Brentano geometry. The diffractometer was equipped with a Cu Kα (1.54051 Å) radiation source. The morphology of the as deposited foam-based electrodes was observed using a scanning electron microscope (SEM) and elemental analysis was performed by the same microscope equipped with an X-ray energy dispersive spectrometer (EDS). The samples for transmission electron microscope (TEM) were prepared by scratching the as-prepared Zn powders from the Cu foam substrate, followed by dispersing them in hexane and collecting them on the TEM copper grids. High resolution transmission electron microscopy (HRTEM) images and scanning transmission electron microscopy (STEM) studies were conducted by using an FEI Tecnai F20 field emission gun microscope operated at 200 kV with a point-to-point resolution of 0.19 nm, which is equipped with high angle annular dark field (HAADF) and electron energy loss spectroscopy (EELS) detectors.

B. Photoanode preparation

Details on the Si heterojunction solar cell fabrication can be found in Ref. 32. The solar cells were electrically connected via solar tabbing wire and Ag epoxy. The planar series-connected cell structure was subsequently encapsulated by a transparent acrylic laminating tape. This construction maintained structural integrity while providing protection from aqueous media. Excess tape was removed and the photovoltaic structure was stored to protect against mechanical and water degradation. The solar cell structure was attached to the Ni foam and electrical contact was made by metallic wires.

View Article Online
DOI: 10.1039/C7EE01747B

C. Photoelectrochemical device set-up and characterization

CO_2 electroreduction experiments were carried out at ambient conditions in a patented filter-press type electrochemical cell[33], schematically depicted in Fig. 1 and reported in one of our previous studies.[34,35] The cell has three inputs (catholyte, anolyte and CO_2 gas) and two outputs (catholyte and gaseous products; anolyte). Anolyte (1 M KOH) and catholyte (0.5 M $KHCO_3$, pre-electrolyzed at -2 V under nitrogen bubbling to remove metal impurities) solutions were kept in two separated tanks and recirculated continuously into the cell by a dual peristaltic pump to enhance flow dynamics. An ionic transport bipolar membrane divides the cell into two separated anodic (pH = 13.7) and cathodic (pH = 7.5) compartments ensuring no accompanying chemical bias stemming from the pH difference in the cell.[36] A mass flow controller was used to control the CO_2 flow rate entering the system, measured downstream by a volumetric digital flowmeter. When using a Zn foil cathode, CO_2 was bubbled directly in the catholyte solution. The flow of CO_2 gas and electrolytes were kept at 20 mL/min. To test the developed Cu-Zn cathode, the Ni foam catalyst, and the photoanode individually in a three electrode configuration, a Dimensionally Stable Anode plate (DSA) was used as the counter electrode. A leak-free Ag/AgCl 3.4 M KCl reference electrode (RE) was assembled in the polytetrafluoroethylene (PTFE) frame of the cell and placed very close to the working electrode surface. The potential was transformed to the reversible hydrogen electrode (RHE) scale: $E\ (V_{RHE}) = E\ (V_{Ag/AgCl}) + 0.0592 \times pH + 0.197$. The data presented for the electrochemical characterization in aqueous solutions in three-electrode configuration do not include compensation for the series resistance of the solution. The Cu-Zn foam was placed onto a titanium electrode holder in the cathode part of the filter-press cell, which defines an active Cu-Zn surface area of 10 cm^2. The Ni foam was also mounted onto a titanium electrode holder in the anode part of the device defining an active are of 10 cm^2. The electrically attached PV devices had an area of 4 cm^2 each, thus during the photoelectrolysis measurement an area of 16 cm^2 was illuminated.

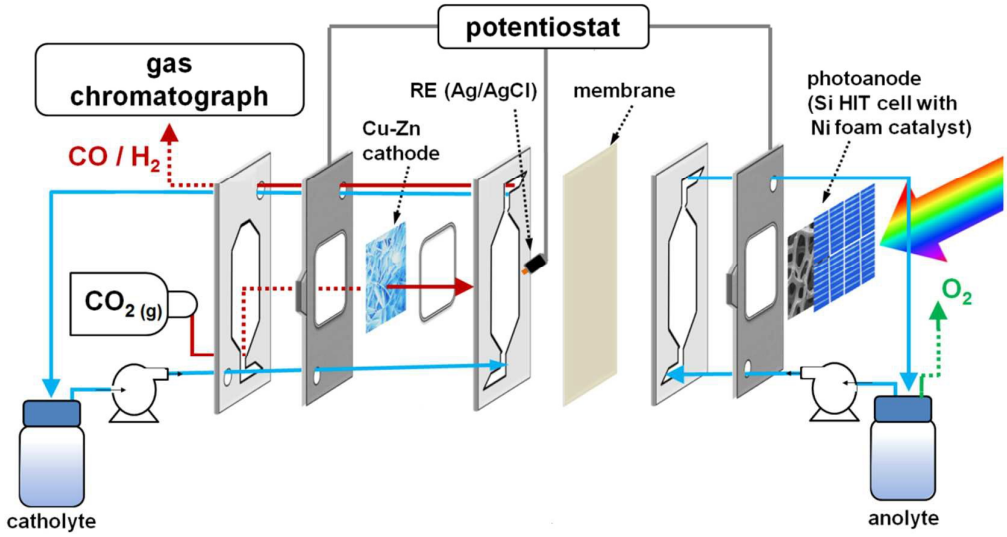

Fig. 1 Schematic illustration of the experimental set-up of the filter-press reactor comprising the Cu-Zn cathode and the Si/Ni foam photoanode.

View Article Online
DOI: 10.1039/C7EE01747B

All photoelectrochemical experiments were conducted using a solar simulator equipped with a 150 W xenon lamp. The intensity of the light source was adjusted to match standard AM 1.5G sunlight at 100 mW/cm^2 intensity. The experiments for the full system assembly were carried out in a two-electrode configuration. The faradaic efficiency to CO and H_2 were calculated using the analysis of the outlet gas by gas chromatography (GC) during potentiostatic measurements. Helium (99.999%) was used as the carrier gas. The calibration of peak area vs. gas concentration was used for the molar quantification of each gaseous effluent. The faradaic efficiency was calculated by determining the number of coulombs needed for each product and then dividing by the total charge passed during the time of the GC sampling according to the flow rate.

III. Results and discussion

A. Cathode based on Cu foam coated with Zn nanoflakes for electrochemical CO_2 reduction

Electrodeposited metallic Zn can be synthetized in a variety of architectures.[37,38] Inspired by the high CO faradaic efficiencies obtained with Zn flake-like structures[18], we intended to coat a Cu foam, as a three-dimensional highly conductive substrate, with nanosized Zn flake catalyst by means of electrodeposition. We first investigated how the duration of the electrodeposition process affect the coverage of the foam, while maintaining a high constant deposition rate (40 mA/cm^2, see Fig. S1, in the ESI). A complete coverage is necessary in order to solely make use of the catalytic properties of Zn and not also of the Cu foam. Cu surfaces are known to favor the production of liquid products, such as formate, and thus, are not adequate when syngas is targeted.[39] In Fig. S2, the comparison of the Cu foam coating after 15, 30, and 60 minute electrodeposition from a 1 M $ZnSO_4$ solution are shown. After 15 and 30 minute electrodeposition, respectively, major parts of the Cu foam surface were still uncovered. Only after one hour the Cu foam was completely coated with Zn flake-like structures, offering a rich active surface area for CO_2-to-syngas catalysis. The full coverage of the Cu foam after one hour electrodeposition has also been validated by chemical composition EELS mapping measurements, shown in Fig. S3. The Cu signal was almost entirely suppressed, which confirms a fully coated Cu foam surface.

The Zn flakes were formed already after shorter electrodeposition times and preserved its shape whilst longer depositions (see high-magnification insets in Fig. S2). According to the high-magnification SEM image shown in Fig. 2(a), the electrodeposition (one hour) resulted in a dense coverage of disordered two-dimensional Zn nanoflake structures with an average diameter of approximately 500 nm. The XRD diffraction pattern in Fig. 2(b) confirmed the highly crystalline nature of the as-prepared Zn electrocatalyst. All the diffraction peaks are well defined and aligned precisely with the reference pattern for Zn (JCPDS card number 03-065-5973). The peaks from the supporting bare Cu foam (corresponding to the Cu JCPDS card number 01-070-3038) are also visible in the diffraction pattern of the Cu-Zn system, as expected.

View Article Online
DOI: 10.1039/C7EE01747B

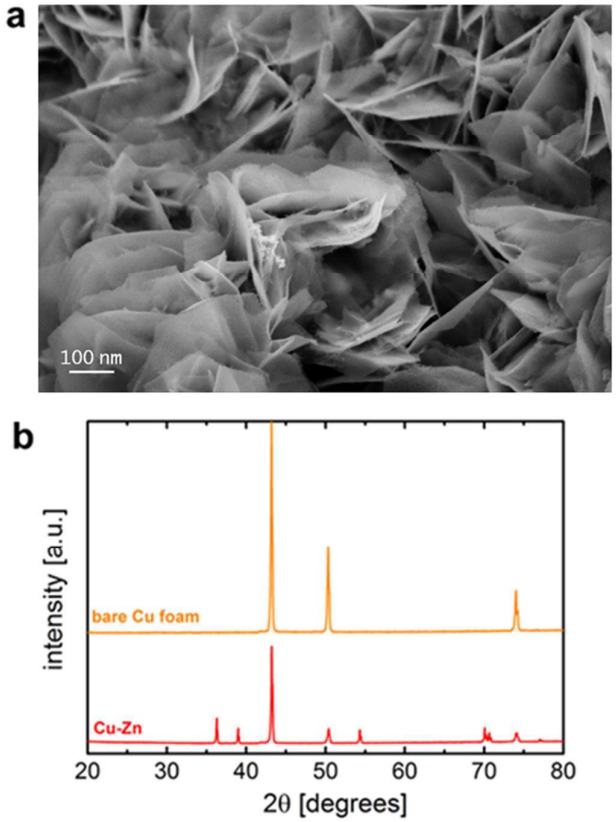

Fig. 2 (a) High-magnification SEM images of the Zn nanoflakes electrocatalyst deposited on Cu foam by electrodeposition. (b) XRD pattern of the bare Cu foam and of the Zn coated Cu foam (Cu-Zn).

The surface of the Zn nanoflake structures was further investigated by means of high-resolution TEM (Fig. 3) in order to gain additional insights into the catalytically active regions. As apparent from this analysis and from the EELS mapping shown in Fig. S3, the nanoflakes are composed of metallic Zn and ZnO. The FFT spectra in Fig. 3(c) and Fig. 3(f) indicate that the material crystallized in the hexagonal Zn phase and in a mixture of hexagonal Zn and hexagonal ZnO phase, respectively. The HRTEM image in Fig. 3a nicely shows two distinct regions: the core region of highly crystalline Zn, which is characterized by continuous metallic Zn and forms the vast majority of the deposited material (red squared region in Fig. 3(a) and Fig. 3(b)); and the surface region composed of a polycrystalline matrix of metallic Zn embedding discontinuously arranged ZnO nanoparticles with diameters of about 5 nm (blue squared region in Fig. 3(a) and Fig. 3(d)). The ZnO/Zn core/shell structures were also confirmed by the inverted FFT image in Fig. 3e, obtained from the FFT spectrum (Fig. 3(f)) of the blue squared region in Fig. 3(a).

View Article Online
DOI: 10.1039/C7EE01747B

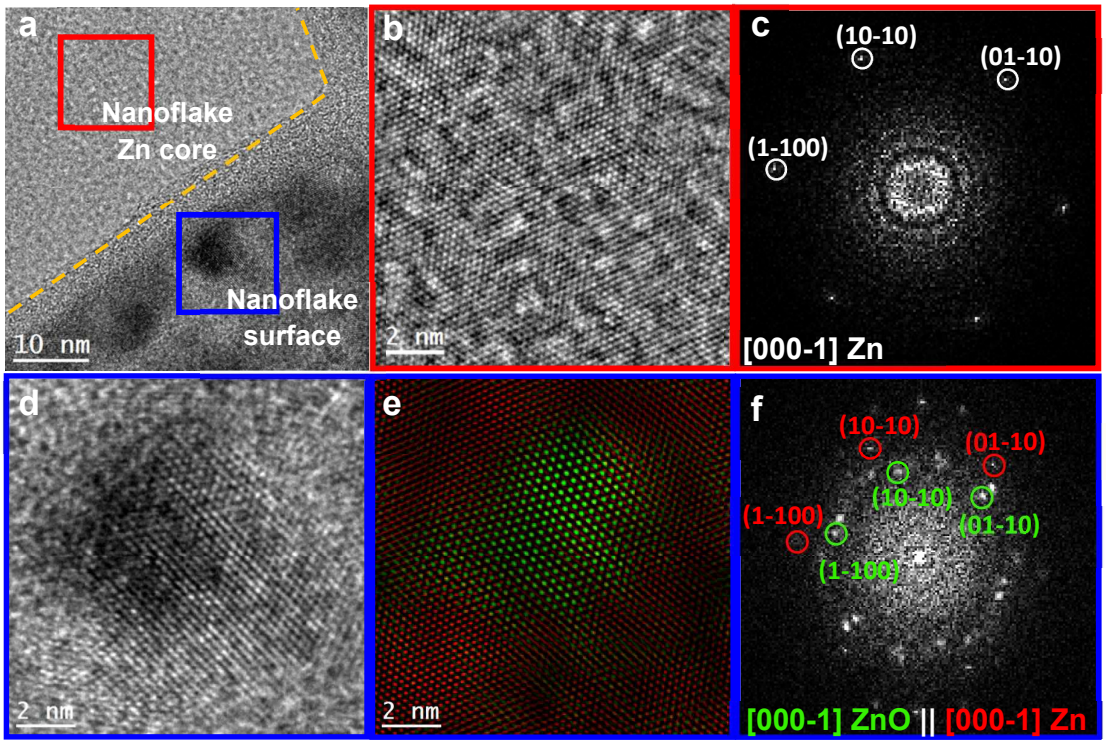

Fig. 3 Left top (a): HRTEM image showing the structural composition of the area near the nanoflake surface. The yellow dashed line shows the boundary between the Zn nanoflake core and the Zn/ZnO polycrystalline periphery. Middle top (b): HRTEM detail of the red squared region. Right top (c): Corresponding FFT spectrum of the red squared region, which indicates that the material crystallizes in the hexagonal Zn phase, as visualized along the [000-1] direction. Left bottom (d): HRTEM detail of the blue squared region. Middle bottom (e): IFFT RGB composite of Zn (red) and ZnO (green). Right bottom (f): Corresponding FFT spectrum of the blue squared region, which indicates that the material crystallizes in a mixture of the hexagonal Zn phase and hexagonal ZnO phase, as visualized along the [000-1] directions.

In particular, Fig. 3(e) illustrates that in the periphery region of the nanoflake, ZnO nanoparticles (green structures) are embedded by a metallic Zn background (red structures). It is well known that metallic Zn can be readily oxidized in the presence of air or moisture. As reported elsewhere, even drying as-prepared Zn samples under vacuum immediately after electrodeposition and keeping them in argon protected environment could not prevent the oxidation of the Zn surface and the formation of a thin (~ 10 nm) ZnO layer at the surface.[17] The reason why in this study the ZnO crystallized into nanoparticles is difficult to clarify. Here in-situ TEM measurements of the electrodepostion of Zn and its phase evolution at atmosphere could give additional insights. Further respective tests were planned and reported elsewhere.[40]

The electrochemical activity of the as-produced Cu-Zn cathode towards CO_2RR was evaluated using constant potential electrolysis in the fluidic filter-press type electrochemical cell shown in Fig. 1 using a three-electrode configuration. A 0.5 M potassium bicarbonate ($KHCO_3$) aqueous electrolyte solution saturated with CO_2 (pH = 7.5) was flown (recirculation flow rate of 20 ml/min) on one side of the cathode. On the

View Article Online
DOI: 10.1039/C7EE01747B

other side, pure CO_2 gas was flown through the Zn coated macroporous three-dimensional Cu-foam (flow rate of 20 ml/min) in order to circumvent the solubility limit in the electrolyte and thus, improve the availability of the three phase interfaces, i.e. the meeting point of CO_2 gas – liquid electrolyte – electrode for CO_2RR catalysis. A similar cell design to the one depicted in Fig. 1 has been proposed also by Kenis et al. and Newman et al. in order to address the CO_2 solubility issue and improving the CO current densities.[41,42]

Fig. 4(a) displays the potentiostatic measurements, which were conducted at different potentials in the range of 0 V_{RHE} to -0.9 V_{RHE} over the course of one hour.

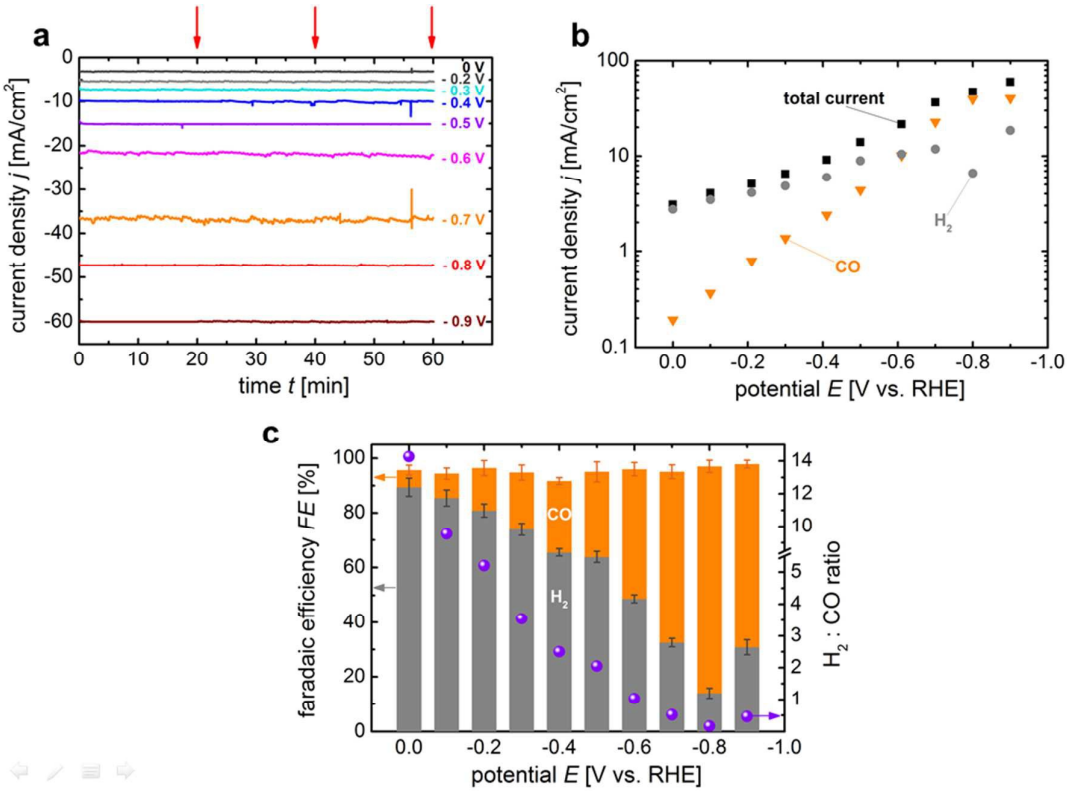

Fig. 4 (a) Chronoamperometry measurements for 10 different potentials (0 V up to -0.9 V) for the Cu-Zn cathode. The red arrows indicate when the gas phase samples were taken. For the sake of readability, the measurement for -0.1 V_{RHE} is not shown here. (b) Total and partial cathodic CO and H_2 current densities, respectively, during CO_2RR plotted on a logarithmic scale over the applied cathodic potential. (c) Left y-axis: Faradaic efficiencies of CO and H_2 at different potentials. Right y-axis: Respective H_2:CO ratios for the investigated potential range. The error bars in (c) are standard deviations obtained from 3 experimental repeats. All measurements were conducted at a CO_2 and electrolyte flow rate of 20 ml/min.

The Cu-Zn cathode shows a very stable operation for all applied potentials. The average total current densities measured at each potential over the time of electrolysis are plotted as a function of the applied potential in Fig. 4(b) (black squares). The data shows an increase in the magnitude of the cathodic current density with increasing cathodic potential, as expected. In Fig. S4 the average current density points are overlaid with the cyclic voltammogram obtained prior to the potentiostatic experiments for comparison. As apparent, the potentiostatic data is consistent with the CV. Figure S4 also evidences

View Article Online
DOI: 10.1039/C7EE01747B

the high activity of the Cu-Zn cathode towards CO_2RR, as the cathode exhibited a significantly higher current density under CO_2 flow than under Ar flow.
The high stability of the Cu-Zn cathode was further confirmed by SEM and XRD measurements and operation stability testing, respectively (see Fig. S5 and S10, respectively, in the ESI). The Zn nanoflakes preserved its shape after electrolysis for one hour at -0.8 V_{RHE} and the XRD pattern were identical before and after the one hour electrolysis operation.

Partial current densities of the CO_2 reduction products are plotted in Fig. 4(b) and were calculated on the basis of GC analysis (normalized on the basis of geometrical surface area). The two primary products under testing conditions were CO from the reduction of CO_2 and H_2 as a byproduct from the concurrent proton reduction reaction. Figure 4(c) displays the faradaic efficiencies of CO and H_2, which were calculated assuming a two-electron transfer for their production. A very high selectivity of the syngas products was achieved, as the total faradaic efficiency was close to 100 % in the investigated potential range. The highest faradaic efficiency of CO was 85 % at a potential of -0.8 V_{RHE} along with an impressive CO current density of 39.4 mA/cm^2 (Fig. 4(b)). Although our cathode development targeted syngas production, the herein achieved partial current density for selective CO production is the highest ever reported for an earth-abundant Zn catalyst at such low overpotentials. Furthermore, as can be deduced from the right ordinate in Fig. 4(b), the H_2:CO ratio can be adjusted very precisely in the range between 5 and 0.5. These syngas ratios are highly suitable for further thermocatalytic conversion to, for instance, ammonia ($\geq$ 3:1), methanol and light olefins ($\geq$ 2:1), waxes and diesel ($\leq$ 2:1), aldehydes and higher alcohols (1.5:1), dimethyl ether, oxo alcohols and acetic acid (1:1), or polycarbonates ($\leq$ 0.5:1).[8] Tunable H_2:CO ratios (between 1:0.5 and 1:1) have also been reported elsewhere,[43] however with significantly lower partial current densities and using expensive catalyst materials such as palladium. The outstanding selectivity towards syngas production was attributed to the unique combination of Zn nanoflake structures supported by the 3D Cu foam. In particular, this marriage was conducive to a much larger contact area between the catalyst and the electrolyte and integrated in the flow reactor design, it additionally ensured a facile transport of reactants (CO_2 and electrolyte) as well as products (CO and H_2).

Among Zn catalysts for CO_2RR, high selectivities have been reported only for CO production so far. In these studies, H_2 evolution has been suppressed either by the presence of chloride ions at the Zn catalyst surface[18] (not present in our study) or by a high density of active stepped sites in nanostructured catalysts.[17] The systematically adjustable H_2:CO ratios measured in our study may result from the morphology and composition of the as-formed Zn nanoflakes. In contrast to the results on increased H_2 suppression from CO_2 reduction for stepped sites, shown for Zn dendrite structures[17] and other catalyst materials such as Cu[44] and Pb[45], our Zn nanoflake structures did not hamper H_2 production to such an extent, despite a high density of stepped sites as compared with a flat catalyst surface. In Fig., S6 the faradaic efficiencies for CO and H_2 production from CO_2RR measured for a flat Zn foil cathode are shown. As apparent, the production of H_2 was amplified compared to our developed Cu-Zn cathode (see Fig. 4(c)), however, not as drastically as presented in the aforementioned related studies. We therefore speculate that the origin of the observed activity towards H_2 production, i.e. solely partial suppression of H_2 production lies in the ZnO nanoparticles embedded in the metallic Zn matrix at the surface of the nanoflakes (see Fig. 3). These ZnO/Zn core/shell structures presumably play a major role in the proton reduction reaction and

View Article Online
DOI: 10.1039/C7EE01747B

favor H_2 generation, especially for lower applied potentials. At higher potentials, i.e. more reducing conditions, ZnO_x might still be catalytically active, although partially reduced. This is confirmed by a decreasing H_2 production and an increasing CO production with increasing potential (up to a maximum CO current density imposed by the limiting CO_2 solubility, see Fig. 4(b) and (c)). Enhanced H_2 production through the decoration of ZnO nanoparticles has already been observed for ZnS and CdS nanocomposites as well.[46,47]

B. Photoanode composed of Si heterojunction solar cell and Ni foam as oxygen evolution reaction catalyst

In view of a stand-alone device for CO_2RR, also OER must be efficient and driven by sunlight energy. For this purpose, we investigated a photoanode system, which consisted of a Ni foam as OER catalyst and a Si heterojunction solar cell as light absorber. The reactor device was designed such that the light directly enters the photoanode without being attenuated by a surrounding medium, e.g. the electrolyte or gas bubbles (see Fig.1). The layer stack used for the deposition of the Si heterojunction solar cells, as well as the photocurrent-density behavior of the photoanode (Si/Ni foam) in three-electrode configuration in 1 M KOH are shown in Fig. S7. Bare Ni foam is known to be an efficient OER catalyst[48], also due to its very large surface-to-volume ratio of 6.900 m^2/m^3. The water-oxidation behavior of the foam alone is shown in Fig. 5(a). The cyclic voltammetry measurements without the photoabsorbing Si cell were conducted in order to provide a measure of the overpotentials of OER in 1 M KOH and in 0.5 M $KHCO_3$ at a scan rate of 10 mV/s. As can be deduced from Fig. 5(a), an overpotential of 375 mV was required to produce 10 mA/cm^2 in 1 M KOH, consistent with results on Ni based anodes.[49] In comparison, an overpotential of 770 mV was required in 0.5 M $KHCO_3$ to produce the same current density of 10 mA/cm^2.

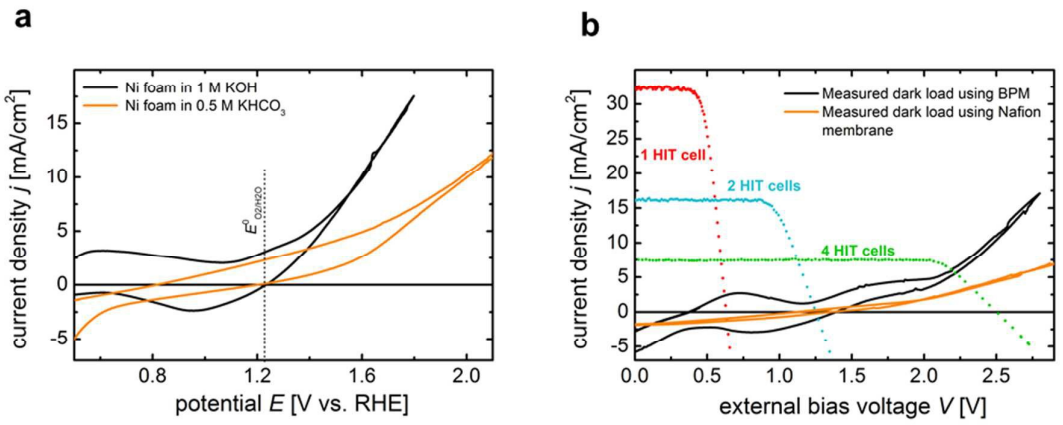

Fig. 5 (a) Performance of the Ni foam towards oxygen evolution reaction (OER) evaluated in a three-electrode configuration by means of cyclic voltammetry measurements at a scan rate of 10 mV/s in 1 M KOH (black curve) and in 0.5 M $KHCO_3$ (orange curve) without correction for uncompensated resistance. The measurements were conducted at a scan rate of 10 mV/s. (b) Overall polarization characteristics for CO_2RR reaction and OER using the Cu-Zn cathode and the Ni foam anode in a two-electrode BPM configuration (0.5 M $KHCO_3$/BPM/1 M KOH) (black curve) as well as in the two-electrode Nafion configuration (0.5 M $KHCO_3$/Nafion/0.5 M $KHCO_3$) (orange curve). The measurements were conducted with 20ml/min CO_2 and electrolyte flow rate and 10 mV/s scan rate. The overlaid current density-voltage characteristics of the applied silicon HIT solar cell as single (red dotted curve) and as series-connected (two cells,

View Article Online
DOI: 10.1039/C7EE01747B

blue dotted curve; four cells, green dotted curve) photovoltaic device were measured under of simulated AM1.5G illumination.

The usage of different catholyte and anolyte electrolytes, separated by a bipolar membrane (BPM), therefore seems to be the more efficient choice for the full device set-up. For the operation of CO_2RR and OER in the same electrolyte, a cation-exchange membrane, such as Nafion, could be applied to separate catholyte and anolyte compartment. Both options have been tested in our filter-press cell set-up. In Fig. 5(b) the overall polarization behavior of the Cu-Zn cathode and the Ni foam anode (dark load) measured in a two-electrode BPM (0.5 M $KHCO_3$/BPM/1 M KOH) (black) and a two-electrode Nafion membrane (0.5 M $KHCO_3$/Nafion/0.5 M $KHCO_3$) (orange) configuration, respectively, are shown. As expected, the configuration using a BPM exhibits an increased performance with respect to lower cell voltages at increasing current densities. This becomes even clearer when the illuminated current density-voltage (*j-V*) curves of the applied Si heterojunction solar cells in single and series-connection configuration are overlaid. As apparent from Fig. 5(b), neither the photovoltage provided by one single solar cell (627 mV) (red), nor the photovoltage of two in-series connected Si cells (1248 mV) (blue) would be sufficient to drive the full device bias-free. Only the series-connection of four Si heterojunction solar cells would provide enough photovoltage (2496 mV) (green) to exhibit CO_2RR and OER without any additional power other than the sun. As displayed in Fig. 5(b), the conjunction of the high-voltage photovoltaic (PV) structure with the electrochemical dark load using BPM lies at a bias-free CO_2RR current-density of 5.1 mA/cm^2 (crossing point at 2.21 V) can be predicted (normalized to the total illuminated area of the PV cells). In contrast, the system using the same electrolyte with Nafion membrane would only exhibit 3.4 mA/cm^2. This is due to the large overpotential for the Ni foam catalyst to drive OER in near neutral pH. The interconnections of the Si HIT solar cells in our experimental set-up increased the series resistance, which resulted in a decrease of the fill factor of the series-connected PV structures (blue and green curves in Fig. 5(b)). Nevertheless, as apparent from Fig. 5(b), in the case of the high voltage solar cell (4 HIT cells in series), the conjunction point with the electrochemical dark load (BPM configuration) lied near the maximum power point of the PV device. Thus, it can be estimated that the decreased fill factors will not significantly impair the performance of the integrated photovoltaic-electrochemical (PV-EC) device.

The influence of the membrane in systems enabling CO_2RR with respect to faradaic efficiencies, stability, and ion transport processes was investigated in several studies already.[42,50-52] It was shown that cation exchange membranes (Nafion) and anion exchange membranes (AEM), although they exhibit less additional membrane-derived voltage losses, suffer more from crossover of ions than BPM membranes. This introduces pH instability and contaminations in the presence of different catholyte and anolyte electrolytes during CO_2RR that affect the faradaic efficiency and selectivity at high current densities. For an efficient CO_2RR, these systems demand a design allowing for recycling of the catholyte and anolyte solutions in an auxiliary process and a careful optimization of the two-phase flow at the cathode.[52] BPMs in contrast, offer the advantage of stable complementary cathode and anode catalysis with stable (local) pH values during electrolysis, which is crucial as the product selectivity for many CO_2RR products strongly depends on the local pH near the cathode surface. In fact, a BPM does not allow cations and anions to pass the membrane. Instead, water is dissociated in the interface layer of the BPM. This supplies H+ to the cathode compartment and OH− to

View Article Online
DOI: 10.1039/C7EE01747B

the anode compartment, in a way that the amount of protons and hydroxides produced by the water dissociation at the BPM equals the consumption at the electrodes (assuming perfect selectivity). Such a balancing of the consumed protons and hydroxides at the electrode reactions facilitates a constant pH difference over the membrane.[53]

C. Stand-alone device for solar-driven CO_2RR

Figure 6 shows the current density for bias-free CO_2RR as a function of the operational time under simulated AM1.5 illumination obtained with the device configuration depicted in Fig. 1, i.e. when the Cu-Zn cathode is directly wired to the Si/Ni foam photoanode (4 Si HIT cells in series) without applying an external bias. Photographs of the reactor device under operation are shown in the ESI in Fig. S8.

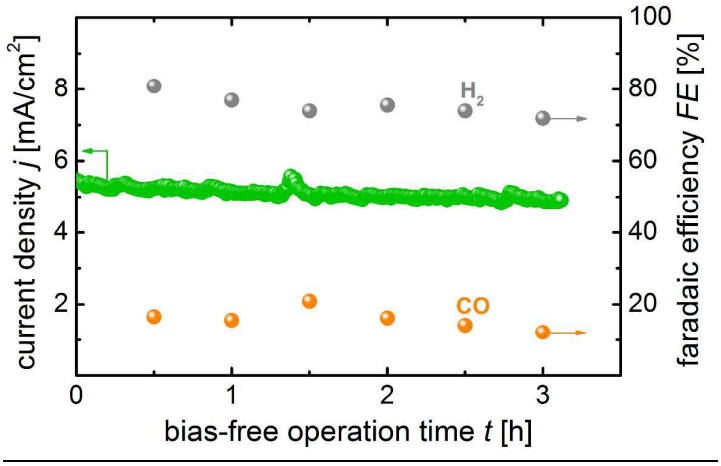

Fig. 6 Bias-free operation of the prototype solar CO_2 conversion reactor (Fig. 1) as a function of the operation time. Left y-axis: Solar-driven CO_2RR current density (normalized to the area of the electrodes in contact with the electrolyte; 10 cm^2) as a function of the operational time using a Si HIT cells/Ni foam photoanode and a Cu-Zn cathode in a two-electrode 0.5 M $KHCO_3$/BPM/1 M KOH configuration under simulated AM1.5G illumination. Right y-axis: Faradaic efficiencies of H_2 and CO production as a function of the operation time.

The solar-driven operational current density j_{op} was 5.0 ± 0.3 mA/cm^2, normalized to the active electrode area (cathode and anode, respectively) of 10 cm^2. The photocurrent density-voltage characteristics of the overall two-electrode device before and after the stability testing are shown in Fig. S9. Both measurements show identical onset potentials and similar current density values at 0 V applied bias, which indicates a good stability of the photoanode structure against corrosion and a stable operation of the overall device. As expected from the behavior depicted in Fig. 4(b) and Fig. 4(c), H_2 and CO were detected as the major gas-phase products during the bias-free CO_2RR operation of the device. The respective faradaic efficiencies of both products are plotted on the right ordinate in Fig. 6. Over the course of 3 hours, the faradaic efficiencies only deceased slightly and were in average 76 % for H_2 and 16 % for CO. Thus, the stability of our stand-alone reactor is in line with other reported bias-free stability tests.[14,49,54] The bias-free measurement further allows to calculate a solar-to-fuel, i.e. a solar-to-syngas conversion efficiency (η_{STF}) for the measured bias-free CO_2RR current density and the corresponding H_2:CO ratio.

View Article Online
DOI: 10.1039/C7EE01747B

We based our calculation on the inherent chemical energy stored in one unit of fuel and derived the exothermic power that can be obtained by combustion of the produced fuels. Taking into account the higher heat value (HHV) and lower heat value (LHV) for H_2 and CO of 286 kJ/mol and 283.5 kJ/mol, respectively, the specific power of the produced products can be obtained as 143330 kW/kg for H_2 and 10125 kW/kg for CO (under the assumption of an interval duration of 1 second). Considering that 76 % of the measured bias-free operation current density (5 mA/cm^2) was used to produce H_2 and 16 % to produce CO, leads to a generated product mass of 0.394 µg of H_2 and 1.16 µg of CO (under the assumption of 10 cm^2 area). These values then can be used to calculate the total bias-free power output of the device. According to Eq. 1, η_{STF} is given by

$$\eta_{STF} = \frac{0.394\ \mu g\ H_2 \times 143330\ kW/kg + 1.16\ \mu g\ CO \times 10125\ kW/kg}{\text{total integrated power input}} \qquad (1)$$

where the input power (100 mW/cm^2, for 16 cm^2 illuminated PV area) is the incident light intensity. Thus, the solar-to-fuel efficiency of our device was 4.3 %. Further details on the η_{STF} calculation can be found in the ESI.

Although the achieved efficiency value does not reach the highest solar-to-fuel conversion published to date,[54] it is comparable to other previously reported bias-free CO_2-to-syngas benchmark values for PV−electrode combinations (η_{STF} < 7.0 %).[14,28,30] Unlike these related studies, our integrated device approach, however, solely includes earth-abundant catalyst materials and cheap silicon PV technology and operates under ambient conditions. Moreover, the presented concept also clearly distinguishes itself from proof-of-concept approaches, demonstrating small-scale subassemblies for solar-driven CO_2 reduction.[14,49,55-59] The coupling of pure academic with engineered systems is urgently needed to mature CO_2 recycling processes and open the pathway towards a commercial application. This aspect is successfully addressed by the proposed concept. Additionally, the scalable modular design of the presented device bears great benefits and cross-fertilization for a number of related catalytic and photovoltaic technologies. Thus, our reactor concept for CO_2 conversion is not limited to small active electrode areas,[60,61] or expensive small-scale photovoltaic structures,[49,54,57] but can be adapted to large scale designs.

Nevertheless, from a scientific point of view, further attention should be devoted to increase the CO_2 solubility in aqueous electrolytes. This could be achieved, for instance, by controlling the cell pressure or applying chemical additives and/or ionic liquid solutions.[62,63] From a more engineering point of view, the evaluation of different approaches for the upscaling of the active surface areas will be crucial for future commercial applications[48] and are currently under investigation in our labs. In this regard, a detailed analysis of the electrical resistivity of the components in the complete integrated solar reactor device will be vital in order to systematically improve its operation performance.[64,65] Furthermore, different strategies for the separation of CO_2 gas from syngas, such as chemical absorption and adsorption, respectively,[66,67] membrane separation,[68] or carbonation/calcination[69] must be further evaluated regarding their applicability and energy requirements in view of a future commercialization.

For a successful application of the artificial photosynthesis concept in a commercial system or product, the final metric of viability is the cost of produced fuel. Several studies addressed the costs and life-cycle analysis for technologies aiming at CO_2 re-use

View Article Online
DOI: 10.1039/C7EE01747B

fuel products.[70,71] These studies show that, among others, the conversion efficiency is the most sensitive parameter to lower the cost of produced fuel.

Therefore, it is vital to evaluate whether the bias-free concept, i.e. solely solar-driven concept offers the best solution regarding productivity or, if it is worth to consider a scenario in which the presented solar CO_2RR system is driven by an external bias to produce a higher operational current density. Based on the current density-voltage curves in Fig. 5(b) of the solar cells and the electrochemical dark load, one can estimate to what extend an additional bias would affect the operation of the solar CO_2RR device. As apparent, an operation current density of 15 mA/cm^2 exemplarily can be achieved by using two HIT cells (blue dotted curve in Fig. 5(b)) and by additionally biasing the system with 1.7 V. In this case, a surplus power of 255 mW (1,7 V * 15 mA/cm^2 for 10 cm^2) would have to be applied to the system. A rough approximation of the respective faradaic efficiencies for H_2 and CO at this operation current density can be deduced from Fig. 4(b) and (c). At -0.5 V the Cu-Zn cathode exhibited 15 mA/cm^2 along with faradaic efficiencies of 64 % and 31 % for H_2 and CO, respectively. Following the calculation described in the ESI, this would correspond to a production of 6.9 µg/s of CO and 0.9 µg/s of H_2. Taking into account the reduced illuminated area for two HIT cells (8 cm^2) a η_{STF*} value of 20.1 % can be estimated for such a biased system. The corresponding stability measurement of the biased solar CO_2 conversion operation (over 10 hours of operation) was performed in our prototype reactor (using two HIT cells) and is shown in the ESI in Fig. S10. The measured faradaic efficiencies for CO and H_2 were in good agreement with the approximated values. While Fig. 6 shows the proof-of-concept experiment to demonstrate bias-free operation, Fig. S10 additionally illustrates the durability of our prototype device regarding photocurrent density and catalytic activity.

In this scenario, the extra bias could be provided by the energy surplus generated by renewable power plants during solar irradiation in periods of low electricity demand. Consequently, the herein proposed PV-EC based system presents an attractive alternative to the currently applied systems for surplus energy storage/usage, such as pumped hydroelectric storage (70-80% efficiency), ion lithium batteries (92-95 % efficiency), or power-to gas based on alkaline and PEM electrolyzers (65-70 % efficiency). Our PV-EC device for solar CO_2RR could be applied during solar irradiation to consume surplus energy and store/convert it into syngas with an efficiency of 83.4 % using two HIT solar cells (212.7 mW/255 mW), for instance.

These examples on the one hand side show the high flexibility that offers our PV-EC device concept for CO_2 re-use, and on the other hand side outline its viability regarding novel energy storage technologies. The presented protoype device therefore may pave the way for future lines of work, which will be needed to address efficiency improvements and technoeconomical questions while assessing its cost competiveness.

IV. Conclusions

In this study we developed a prototype device for solar-driven CO_2-to-syngas conversion using state-of-the-art silicon photovoltaics and a highly selective and earth-abundant cathode with an active reaction area of 10 cm^2. The stand-alone reactor device exhibited a stable and bias-free operation with a solar-to-syngas conversion efficiency of 4.3 %. We presented in detail the structural and electrochemical characteristics of the integrated device components, i.e. the Zn coated Cu foam cathode and the high voltage

View Article Online
DOI: 10.1039/C7EE01747B

silicon based photoanode. In this regard, we provided evidence that metallic foams can be applied as high performance electrodes for the electrochemical CO_2 reduction process. Stable and tunable hydrogen-to-carbon monoxide (H_2:CO) ratios along with high CO faradaic efficiencies of up to 85 % and CO current densities of 39.4 mA/cm^2 have been demonstrated using a Cu foam cathode coated with nanoflake Zn catalyst structures. Furthermore, the application of Si heterojunction solar cells in combination with a Ni foam as efficient photoanode structure for OER has been evaluated. The series-connection of four silicon solar cells provided sufficient photovoltage in order to drive CO_2RR and OER without additional bias. Finally, with the integration of the developed cathode and photoanode in a flow-cell reactor device for solar-driven syngas production, a bias-free current density of 5.0 mA/cm^2 was generated.

Acknowledgements
We thank M. Biset-Peiró and S. Murcia-López for their contributions to this work. Authors from IREC and UB thank Generalitat de Catalunya for financial support through the CERCA Programme, M2E (2014SGR1638), and XaRMAE network. IREC also gratefully acknowledges additional support by the MINECO coordinated project TNT-Fuels, by Repsol, S.A., and by the European Regional Development Funds (ERDF, FEDER). P.T, J.A and J.R.M acknowledge funding from the Spanish MINECO coordinated projects between IREC and ICN2 TNT-FUELS and e-TNT (MAT2014-59961-C2-2-R). ICN2 acknowledges support from the Severo Ochoa Program (MINECO, Grant SEV-2013-0295). UPC acknowledges support from the Spanish government under project ENE2013-48629-C4-1-R.

Contributions
F.U. conceived the project and designed the experiments. F.U. carried out the structural (SEM, XRD), photovoltaic, electrochemical, and photoelectrochemical experiments. P.T. and J.A. performed the structural characterization. N.M.C. and T.A. carried out the metallic zinc synthesis. C.V. and L.G.G. prepared the silicon solar cells. F.U. and J.R.M. interpreted data. F.U. wrote the manuscript. All authors participated in discussions and contributed to editing of the manuscript.

Competing financial interests
The authors declare no competing financial interests.

View Article Online
DOI: 10.1039/C7EE01747B

References

[1] M. Z. Jacobson, Energy Environ. Sci., 2009, **2**, 148-173.
[2] K. Li, X. An, K. H. Park, M. Khraisheh, and J. Tang, Catalysis Today, 2014, **224**, 3-12.
[3] K. Li, B. Peng, and T. Peng, ACS Cat., 2016, **6**, 7485−7527.
[4] Z.-L. Wang, C. Li, and Y. Yamauchi, Nano Today, 2016, **11**, 373–391.
[5] M. Ma, B. J. Trześniewski, J. Xie, and W. A. Smith, Angew. Chem. Int. Ed., 2016, **55**, 9748–9752.
[6] K. P. Kuhl, T. Hatsukade, E. R. Cave, D. N. Abram, J. Kibsgaard, and T. F. Jaramillo, J. Am. Chem. Soc., 2014, **136**, 14107-14113.
[7] Y. Wang S. Fan, B. AlOtaibi, Y. Wang, L. Li, and Z. Mi, Chem. Eur. J., 2016, **22**, 8809-8813.
[8] M. Wenzel, L. Rihko-Struckmann, and K. Sundmacher, AIChE, 2017, **63**, 15-22.
[9] I. Wender, Fuel Process. Technol., 1996, **48**, 189-297.
[10] Y. Cao, Z. Y. Gao, J. Jin, H. C. Zhou, M. Cohron, H. Y. Zhao, H. Y. Liu and W. P. Pan, Energy Fuels, 2008, **22**, 1720-1730.
[11] H. Mistry, R. Reske, Z. H. Zeng, Z. J. Zhao, J. Greeley, P. Strasser, and B. R. Cuenya, J. Am. Chem. Soc., 2014, **136**, 16473-16476.
[12] P. Kang, Z. F. Chen, A. Nayak, S. Zhang, and T. J. Meyer, Energy Environ. Sci., 2014, **7**, 4007-4012.
[13] T. Hatsukade, K. P. Kuhl, E. R. Cave, D. N. Abram, and T. F. Jaramillo, Phys.Chem.Chem.Phys., 2014, **16**, 13814-13819.
[14] M. Schreier, L. Curvat, F. Giordano, L. Steier, A. Abate, S. M. Zakeeruddin, J. Luo, M. T. Mayer, and M. Grätzel, Nat. Commun., 2015, **6**, 7326.
[15] Y. Hori, H. Wakebe, T. Tsukamoto, and O. Koga, Electrochim. Acta, 1994, **39**, 1833-1839.
[16] S. Ikeda, A. Hattori, K. Ito, and H. Noda, Electrochemistry, 1999, **67**, 27−33.
[17] J. Rosen, G. S. Hutchings, Q. Lu, R. V. Forest, A. Moore, and F. Jiao, ACS Cat., 2015, **5**, 4586−4591.
[18] F. Quan, D. Zhong, H. Song, F. Jia, and L. Zhang, Mater. Chem. A, 2015, **3**, 16409-16413.
[19] J. Lee, Y. Kwon, R. L. Machunda, and H. J. Lee, Chem. Asian J., 2009, **4**, 1516-1523.
[20] C. Battaglia, A. Cuevas, and S. De Wolf, Energy Environ. Sci., 2016, **9**, 1552-1576.
[21] M. Taguchi, A. Yano, S. Tohoda, K. Matsuyama, T. Nishikawa, K. Fujita, and E. Maruyama, IEEE J. Photovoltaics, 2014, **4**, 96.
[22] H. Zhong, J. Wang, F. Meng, and X. Zhang, Angew. Chem. Int. Ed., 2016, **128**, 10091–10095.
[23] J. Wang, K. Li, H.-X. Zhong, D. Xu, Z.-L. Wang, Z. Jiang, Z.-J. Wu, and X.-B. Zhang, Angew. Chem. Int. Ed., 2016, **54**, 10530 –10534.
[24] J. Wang, H.-X. Zhong, Z.-L. Wang, F.-L. Meng, and X.-B. Zhang, ACS Nano, 2016, **10**, 2342-2348.
[25] J. Wang, H.-X. Zhong, Y.-L. Qin, and X.-B. Zhang, Angew. Chem. Int. Ed., 2013, **125**, 5356-5361.
[26] F. Meng, H.-X. Zhong, D. Bao, J. Yan, and X.-B. Zhang, J. Am. Chem. Soc., 2016, **138**, 10226–10231.
[27] M. R. Singh and A. T. Bell, Energy Environ. Sci., 2016, **9**, 193-199.
[28] M. Asadi, K. Kim, C. Liu, A. V. Addepalli, P. Abbasi, P. Yasaei, P. Phillips, A. Behranginia, J. M. Cerrato, R. Haasch, P. Zapol, B. Kumar, R. F. Klie, J. Abiade, L. A. Curtiss, and A. Salehi-Khojin, Science, 2016, **353**, 467-470.
[29] J. L. White, J. T. Herb, J. J. Kaczur, P. W. Majsztrik, A. B. Bocarsly, J. CO2 Util., 2014, **7**, 1-5.
[30] D. Marxer, P. Furler, M. Takacs, and A. Steinfeld, Energy Environ. Sci., 2017, **10**, 1142-1149.
[31] N. Alias and A. A. Mohammed, J. King Saud Univ. Eng. Sci., 2015, **27**, 43-48.
[32] M. Colina, A. Belén Morales-Vilches, C. Voz, I. Martín, P. R. Ortega, and R. Alcubilla, IEEE J. Photovolt., 2015, **5**, 805-811.
[33] M. D. Hernández-Alonso, G. Penelas-Pérez, T. Andreu, E. Irtem, A. Parra, C. Fábrega, and

View Article Online
DOI: 10.1039/C7EE01747B

J. R. Morante, Filter-press photoelectrochemical water oxidation and CO_2 reduction cell, Patent WO/2016/097247, 23 June 2016.
[34] E. Irtem, M. D. Hernández-Alonso, A. Parra, C. Fàbrega, G. Penelas-Pérez, J. R. Morante, and T. Andreu, Electrochem Acta, 2017, **240**, 225-230.
[35] E. Irtem, T. Andreu, A. Parra, M. D. Hernández-Alonso, S. García-Rodríguez, J. M. Riesco-García, G. Penelas-Pérez, and J. R. Morante, J. Mater. Chem. A, 2016, **4**, 13582-13588.
[36] N. M. Vargas-Barbosa, G. M. Geise, M. A. Hickner, and T. E. Mallouk, ChemSusChem, 2014, **7**, 3017-3020.
[37] R. Y. Wang, D. W. Kirk, and G. X. Zhang, J. Electrochem. Soc., 2006, **153**, C357−C364.
[38] D. Grier, E. Ben-Jacob, R. Clarke, and L. M. Sander, Phys. Rev. Lett., 1986, **56**, 1264-1267.
[39] S. Min, X. Yang, A.-Y. Lu, C.-C. Tseng, M. N. Hedhili, L.-J. Li, and K.-W. Huang, Nano Energy, 2016, **27**, 121-129.
[40] B. Han, K. A. Stoerzinger, V. Tileli, A. D. Gamalski, E. A. Stach, and Y. Shao-Horn, Nat. Mat., 2017, **16**, 121-126.
[41] D. T. Whipple, E. C. Finke, and P. J. A. Kenis, Electrochem. Solid State Lett., 2010, **13**, D109–D111.
[42] C. Delacourt, P. L. Ridgway, J. B. Kerr, and J. Newman, J. Electrochem. Soc., 2008, **155**, B42–B49.
[43] W. Sheng, S. Kattel, S. Yao, B. Yan, Z. Liang, C. J. Hawxhurst, Q. Wu, and J. G. Chen, Energy Environ. Sci., 2017, **10**, 1180-1185.
[44] C. W. Li and M. W. Kanan, J. Am. Chem. Soc., 2012, **134**, 7231−7234.
[45] C. H. Lee and M. W. Kanan, ACS Catal., 2015, **5**, 465−469.
[46] A. Wu, L. Jing, J. Wang, Y. Qu, Y. Xie, B. Jiang, C. Tian, and H. Fu, Sci. Rep., 2015, **5**, 8858.
[47] S. Mukhopadhyay, I. Mondal, U. Pal, and P. S. Devi, Phys. Chem. Chem. Phys., 2015, **17**, 20407-20415.
[48] B. Turan, J.-P. Becker, F. Urbain, F. Finger, U. Rau, and S. Haas, Nat. Comm. 2016, **7**, 12681.
[49] X. Zhou, R. Liu, Y. Chen, E. Verlage, S. A. Francis, N. S. Lewis, and C. Xiang, ACS Energy Lett., 2016, **1**, 764–770.
[50] D. A. Vermaas and W. A. Smith, ACS Energy Lett., 2016, **1**, 1143-1148.
[51] Y. C. Li, D. Zhou, Z. Yan, R. H. Goncalves, D. A. Salvatore, C. P. Berlinguette, and T. E. Mallouk, ACS Energy Lett., 2016, **1**, 1149-1153.
[52] Q. Lu and F. Jiao, Nano Energy, 2016, **29**, 439-456.
[53] D. A. Vermaas, M. Sassenburg, W. A. Smith, J. Mater. Chem. A, 2015, **3**, 19556–19562.
[54] M. Schreier, F. Héroguel, L. Steier, S. Ahmad, J. S. Luterbacher, M. T. Mayer, J. Luo, and M. Grätzel, Nat. Energy, 2017, **2**, 17087.
[55] Y. Sugano, A. Ono, R. Kitagawa, J. Tamura, M. Yamagiwa, Y. Kudo, E. Tsutsumi, and S. Mikoshiba, RSC Adv., 2015, **5**, 54246-54252.
[56] T. Arai, S. Sato, and T. Morikawaa, Energy Environ. Sci., 2015, **8**, 1998-2002.
[57] T. Sekimoto, S. Shinagawa, Y. Uetake, K. Noda, M. Deguchi, S. Yotsuhashi, and K. Ohkawa, Appl. Phys. Lett. 2015, **106**, 073902.
[58] T. Sekimoto, H. Hashiba, S. Shinagawa, Y. Uetake, M. Deguchi, S. Yotsuhashi, and K. Ohkawa, J. Phys. Chem. C, 2016, **120**, 13970−13975.
[59] J. T. Song, H. Ryoo, M. Cho, J. Kim, J.-G. Kim, S.-Y. Chung, and J. Oh, Adv. Energy Mater., 2016, **1601103**, 1-8.
[60] X. Zhang, Z. Wu, X. Zhang, L. Li, Y. Li, H. Xu, X. Li, X. Yu, Z. Zhang, Y. Liang, and H. Wang, Nat. Commun., 2017, **8**, 14675.
[61] J. Wei, Q. Ge, R. Yao, Z. Wen, C. Fang, L. Guo, H. Xu, and J. Sun, Nat. Commun., 2017, **8**, 15174.
[62] M. Ramdin, T. W. de Loos, and T. J. H. Vlugt, Ind. Eng. Chem. Res. 2012, 51, 8149−8177.
[63] B. A. Rosen, A. Salehi-Khojin, M. R. Thorson, W. Zhu, D. T. Whipple, P. J. A. Kenis, and R. I. Masel, Science, 2011, 334, 643-644.
[64] F. Urbain, V. Smirnov, J.-P. Becker, U. Rau, J. Ziegler, B. Kaiser, W. Jaegermann, and F.

View Article Online
DOI: 10.1039/C7EE01747B

Finger, Sol. Energy Mater. Sol. Cells, 2015, **140**, 275-280.
[65] Y. Chen, N. S. Lewis, C. Xiang, ACS Energy Lett., 2016, **1**, 273−280.
[66] M. R. M. Abu-Zahra, L. H. J. Schneiders, J. P. M. Niederer, P. H. M. Feron, and G. F. Versteeg, Int. J. Greenh. Gas Control, 2007, **1**, 37-46.
[67] P. Nugent, Y. Belmabkhout, S. D. Burd, A. J. Cairns, R. Luebke, K. Forrest, T. Pham, S. Ma, B. Space, L. Wojtas, M. Eddaoudi, and M.J. Zaworotko, Nature, 2013, **493**, 80–84.
[68] C.A. Scholes, J. Bacus, G. Q. Chen, W. X. Tao, G. Li, A. Qader, G. W. Stevens, S. E. Kentish, J. Membrane Sci., 2012, **389**, 470-477.
[69] Y. A. Criado, B. Arias, and J. C. Abanades, Energy Environ. Sci., 2017, in press, DOI: 10.1039/c7ee01505d
[70] N. von der Assen , P. Voll , M. Peters , and A. Bardow , Chem. Soc. Rev., 2014, 43, 7982-7994.
[71] J. A. Herron , J. Kim , A. A. Upadhye , G. W. Huber , and C. T. Maravelias , Energy Environ. Sci., 2015, 8, 126-157.